Near-field optics simulation of a solid immersion lens combining with a conical probe and a highly efficient solid immersion lens-probe system

Yuan-Fong Chau, Tzong-Jer Yang, and Din Ping Tsai

Citation: Journal of Applied Physics **95**, 3378 (2004); doi: 10.1063/1.1650541
View online: http://dx.doi.org/10.1063/1.1650541
View Table of Contents: http://scitation.aip.org/content/aip/journal/jap/95/7?ver=pdfcov
Published by the AIP Publishing

Near-field optics simulation of a solid immersion lens combining with a conical probe and a highly efficient solid immersion lens-probe system

Yuan-Fong Chau and Tzong-Jer Yang[a)]
Department of Electrophysics, National Chiao Tung University, Hsinchu 30050, Taiwan, Republic of China

Din Ping Tsai
Department of Physics, National Taiwan University, Taipei, Taiwan, Republic of China

(Received 27 October 2003; accepted 23 December 2003)

A solid immersion lens (SIL) combined with near-field probes which are the conic dielectric probe and the local metallic coating on the SIL probe is designed for optical recording by means of a three-dimensional rather than two-dimensional finite difference time domain method to gain more insight in the near-field distribution. Our computation model is realistic to match the real SIL-probe system. The optical properties of near-field distributions between the SIL probe and recording layers are investigated. A promising idea for fabricating a type of the SIL-probe system is proposed. Results of our designation of an optimal SIL-probe system can achieve higher performance (in terms of high throughput and low reflection of the light beam) for optical data storage and microscopy than the conventional metal NSOM probe or SIL used alone. © *2004 American Institute of Physics.* [DOI: 10.1063/1.1650541]

I. INTRODUCTION

As the demand for data storage capacity continually grows, data storage technologies are being driven to higher area densities. Because they produce small spot size, near-field optical techniques using evanescent light are being developed to overcome the diffraction limit of far-field optics and have been applied to optical data storage achieving high recording densities. In this case, small aperture, scattering points or solid immersion lens (SIL) have been used to record or retrieve small marks beyond the diffraction limit. In particular, Betzig *et al.* first applied a small aperture for magneto-optical recording to record and retrieve small marks.[1] The resolution of the metal coated taper in a scanning near-field optical microscope (SNOM) probe is not limited by the far-field diffraction limit and the resolution is less than 60 nm. However, low efficiency of the throughput of this probe limits the speed if readout and recording. Martin *et al*. adapted an oscillation aperture-less media.[2] Plannar aperture flying heads have also been developed.[3–5] SIL has been applied to magneto-optical recording.[6,7] The SIL system has been analyzed by using numerical simulation and also static experiments.[8,9] An advantage of the SIL lens is high optical throughput, which is several orders of magnitude larger than that of a conventional SNOM probe. However, there is technical difficulty in keeping the position of the relatively large flat bottom of the SIL in the near-field zone of the recoding medium. In order to overcome this issue, a sharp conical shape attached at the bottom of the SIL can improve the position of the SIL probe.[10] Therefore, estimation of the field behavior about the signal readout process includes the interaction of the electromagnetic fields between the near-field probe and the marks is a very important factor in the SIL-probe system. However, analytical methods face difficulty when the SIL-probe system has complicated geometry. Kusato *et al.* first designed a tapered dielectric near-field probes for optical recording using a commercial finite difference time domain (FDTD) code for the FDTD computations.[10] In order to simplify their computational model, a perfect electric conductor as a recorded mark, is set into the dielectric medium in order to calculate the scattered field from the mark. Since metal taken as a perfect conductor[11–14] causes concern that the optic in the near-field region surrounded by metal may not be simulated accurately, and the recording layers regards as a single dielectric medium is not realistic to the real SIL-probe system. For the purpose of improving this problem, the computational model we used is approached to the real system and we designed an alternative tapered probe whose bottom is flat, table shape, coated with a thin metal film on the local surface and $1/n$ wavelength in diameter. This diameter is large enough to propagate the incident light without significant decay of the amplitude and the diameter significantly than the spot size achievable with the SIL uses alone. For conventional optical simulation programs that are not directly transferred to analyze near-field phenomena and some commercial codes can not grasp the detailed properties in SNOM which we intend to realize, we have developed a near-field optical program which is written in Fortran language by a three-dimensional (3D) FDTD[15–17] method basing on the Maxwell's equations to calculate the field distribution around the SIL-probe system. This FDTD method is a very useful method to obtain the field distribution between the probe and the sample in the near-field interaction.[18,19]

In this article, we describe our simulation results on the optical properties of field distribution between the SIL-probe and the recording-layers system. An optical system that combines a SIL with a probe tip exhibits certain merits. The main advantage of this system is small spot size, which is mainly

[a)]Electronic mail: yangtj@cc.nctu.edu.tw

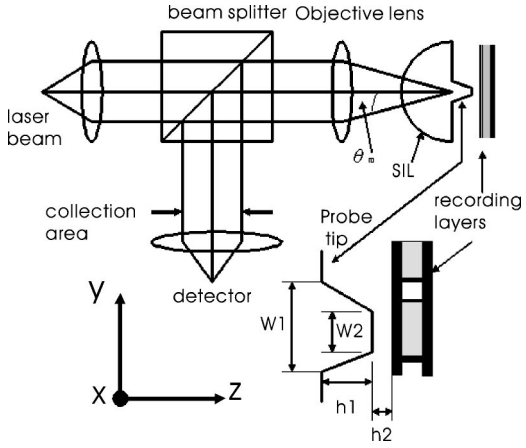

FIG. 1. Simulation model for SIL and probe combination inserted between a focusing objective and the recording-layers.

determined by the size of probe apex, because the light spot illuminating the probe apex is smaller than is possible with fiber base or far-field illumination. Another fundamental advantage of the SIL-probe is in the detection process. In order to fabricate an optimal SIL-probe system, the local surface of SIL base and the local surface of probe tip are coated with metallic thin film. An idea to implement the fabrication of a type of the SIL-probe system is proposed.

II. SIMULATION MODEL

A system using a hemispherical SIL with a conical dielectric probe between an objective lens and the recording layers is shown in Fig. 1, in which the optical spot diameter s in the recording layers is reduced by a factor equal to the refractive index $n_{\text{sil-probe}}$. That is, the full-width-at-$1/e^2$ spot size s is approximately $s=\lambda/\text{NA}_{\text{eff}}$, where NA_{eff} is the effective numerical aperture and λ is the wavelength of laser light in air. For the hemispherical SIL, $\text{NA}_{\text{eff}}=n_{\text{sil}}\sin\theta$, n_{sil} is the refractive index in the SIL, and θ is the angle between the outmost rays and the optic axis. In this system $\text{NA}_{\text{eff}}>1$ can be easily realized with a high index SIL. The SIL is a perfect hemisphere that combined with a conical probe. By placing the flat surface exactly on the focal plane of the objective lens and centering the lens under the objective, the laser beam focused on the optic axis will unrefractly pass the lens and continue to focus directly on the flat surface. The probe, which is in near contact with the recording layers, reduces the wavelength by some factors and produces a small spot size. The reflected light is collected by the objective lens and directed to the detectors. The probe shape can be easily fabricated by using a conventional lithographic technique and applied to a flying head for near-field optical recording. In our simulation model, we assume that the truncated Gaussian light beam is focused throughout a hemispherical lens surface as shown in Fig. 1, and the incident beam on the SIL is simulated in the polarized plane wave. The Gaussian beam is emulated by ten voltage excitation ports on the meshes at the top of the plane in computation-cell space. The incident electric field is a sinusoidal wave. The dimension of each cell are set as $\Delta x=\Delta y=\Delta z=\Delta$ and each time steps $\Delta t\leqslant\Delta/(c\sqrt{3})$ (where c is speed of light). The wavelength of the incident light is $\lambda=633$ nm. The incident linearly polarized light along the y direction is used to illuminate an objective lens of 0.5 NA that focused through the SIL probe and propagating to the recording layers. The focal point in each case is located at the entrance of the probe. The process time of one calculation is about 40–120 min using a personal computer with an Intel Pentium 4 processor (2.4 GHz CPU, 1024 MB DDR RAM). The total number of time steps for computation are 2000 time steps.

III. NUMERICAL RESULTS

A. NSOM image in a SIL-probe system without effects of recording-layers interactions

First, we examine the material for the SIL-probe (LaSFN9 glass; its refractive index $n=1.843$). In order to understand the detailed mechanism for the incident light passing through the SIL probe, the interactions between the SIL probe and recording layers are neglected for simplicity. The calculated intensity distributions in the SIL-probe system without the recording layers are shown in Figs. 2 and 3. An acute probe is chosen to be an aperture angle of 28° and divided the model into $141(x)\times141(y)\times141(z)$ unit cells. The dimension of each cell are chosen as $\Delta x=\Delta y=\Delta z=\Delta=5$ nm. The entrance and the exit diameter of the probe are $w_1=300$ nm and $w_2=100$ nm, respectively. The probe height is $h_1=400$ nm. Although this model is rotational symmetric system, the electric field distributions formed in the two orthogonal cross sections are different from each other due to the difference between the boundary conditions on the

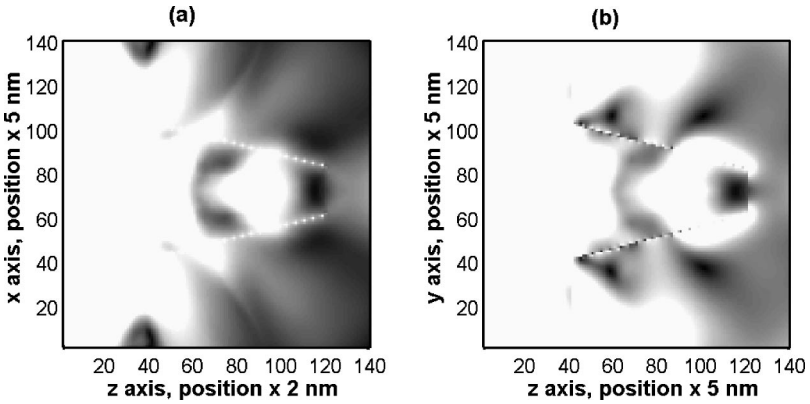

FIG. 2. (a) and (b) show the gray-scaled map of the total electric field modulus on an $x-z$ sectional plane (at $y=71\Delta$) and $y-z$ sectional plane (at $x=71\Delta$) for y-polarization illumination, respectively. In the gray-scaled we used, white signifies higher intensity values.

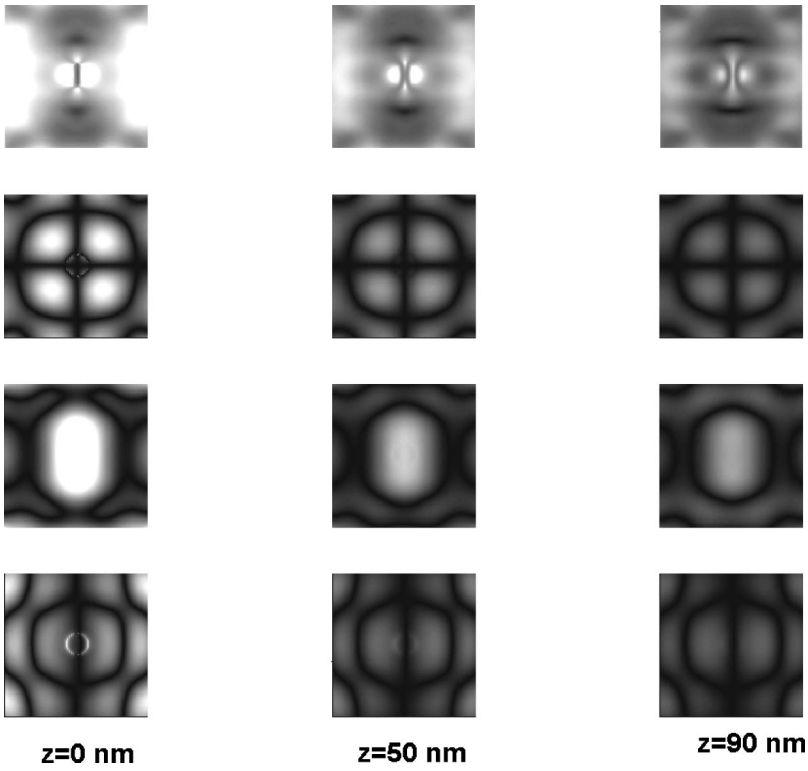

FIG. 3. Distribution of total electric-field and field components in the plane away from probe apex of z=0, 50, 90 nm (from left to right). From top to bottom: $|E_t|$, $4\times|E_x|$, $|E_y|$, $|E_z|$.

edge interface. In the usual experiments, the 3D probes support both polarizations simultaneously. Figures 2(a) and 2(b) present the linear gray-scaled map of the total electric field modulus on $x-z$ sectional plane (at $y=71\Delta$) and $y-z$ sectional plane (at $x=71\Delta$) for *y*-polarization illumination, respectively. In the gray-scaled, white is used to signify higher intensity values. The radiated beam profile in the $x-z$ sectional plane is slightly narrower than that of $y-z$ sectional plane and the field distributions of them including two high-intensity regions along the probe axis. The incident wave is focused on the central part of SIL bottom by an objective lens. The large index of refraction of the LaSFN9 glass reduces the effective wavelength inside the SIL probe and the *y*-direction polarized wave is easily guided down the apex direction of the SIL probe. For both Figs. 2(a) and 2(b), the intensity becomes stronger near the base of the SIL and the conic side of the probe. The light is mainly split into two parts, one escaping from lateral sides at the intersection surface between the SIL and the probe (these far-field components will contribute to illuminate on a large spatial zone), the other one propagating inside the tip as far as this one is wide enough. The reflection light from the conic side of the probe couples with the incident light to become the incomplete standing wave and the light start to escape from the lateral surfaces as long as the diameter of conic shape larger than $(0.27)\lambda/n_{\text{sil-probe}}$ nm. These will also contribute far-field component. The light generated by the apex of the probe is essentially evanescent, since most propagating components escaped laterally before reaching the top of the probe apex. The near-field effect is confined to the surface area located in front of the probe extremity and the illumination process is mainly supported by the evanescent fields in this region. This is a phenomenon of near-field scattering. By way of our simulation in this case we find the electric field distribution of Fig. 2(a) presents a strong field intensity near the central part of the probe apex. The behavior of the $y-z$ sectional

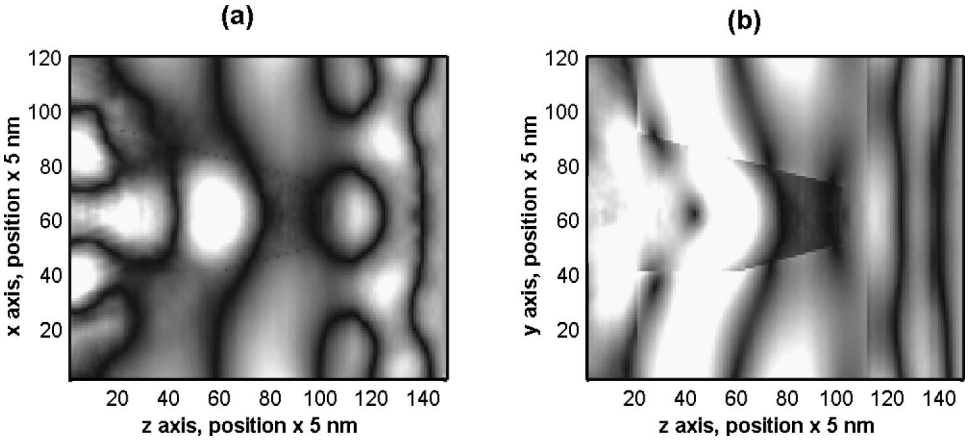

FIG. 4. The scattered electric fields in time domain snap shot of (a) $x-z$ (at $y=61\Delta$) and (b) $y-z$ sectional plane (at $x=61\Delta$), respectively.

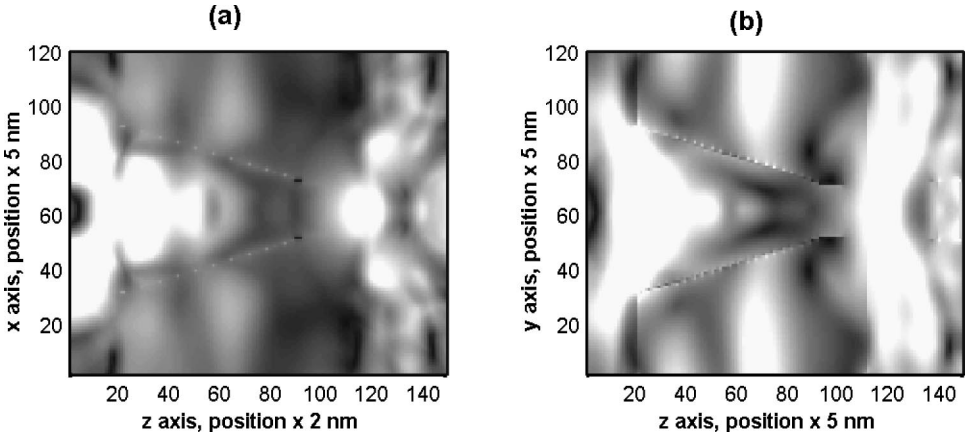

FIG. 5. The steady state electric field intensity plots of (a) the $x-z$ sectional plane and (b) $y-z$ sectional plane, respectively.

plane shown in Fig. 2(b) is found the strongest near the rim of the probe apex and presents the edge enhancement effect. LaSFN9 probes produce a well-confined and intense central spot, from the $x-z$ sectional plane for the y-direction polarization, sometimes with a small central decay due to depolarization effects occurring in the $y-z$ sectional plane. The well-confined spot which size is smaller than $(3/4)\lambda/n_{\text{sil-probe}}$ should be dominant if the probe-surface distance is small enough for an efficient coupling of the evanescent field from the probe to the recording layer.

The polarized incident wave is decayed gradually by the dielectric tip, after exiting the apex of the probe, produces two perpendicularity polarized electric-field components, that is the incident field is entirely polarized along the y axis, the scattered field has also components along the x axis and z axis, respectively. These components produce depolarization at this interface between the probe tip and the air. Figure 3 shows the distributions of total electric-field and field components in the plane away from probe apex of $z=0$, 50, 90 nm (from left to right). From top to bottom: $|E_t|$, $4\times|E_x|$, $|E_y|$, $|E_z|$. The size of each image plane displayed is 600×600 nm^2 in front of the probe. The x component of the electric field is distributed symmetrically along the rim of the probe apex showing four petals distributions much smaller than that of the y and z component. The z component of the electric field is also smaller than the y component of the electric field at the exit plane of the probe apex showing two petals distributions, an interesting enhancement occurs at the rim of the tip apex. Both $|E_x|$ and $|E_z|$ decay rapidly as the distance away from the probe increases. The y component of the electric field leads to propagation mainly in the forward direction along the probe axis. This component is the same as that of the polarization direction of the incident field. The depolarization phenomenon of components is the near-field effect. Consideration of the evanescent decay is of primary importance in the design SIL-probe system. Recall that under the weak scatterer approximation the strongest intensities are found near the center of the tip apex.

B. NSOM image in a SIL-probe system with effects of scattering field from a recording mark

The calculated intensity of images will be discussed in this section when the SIL probe and recording layers are

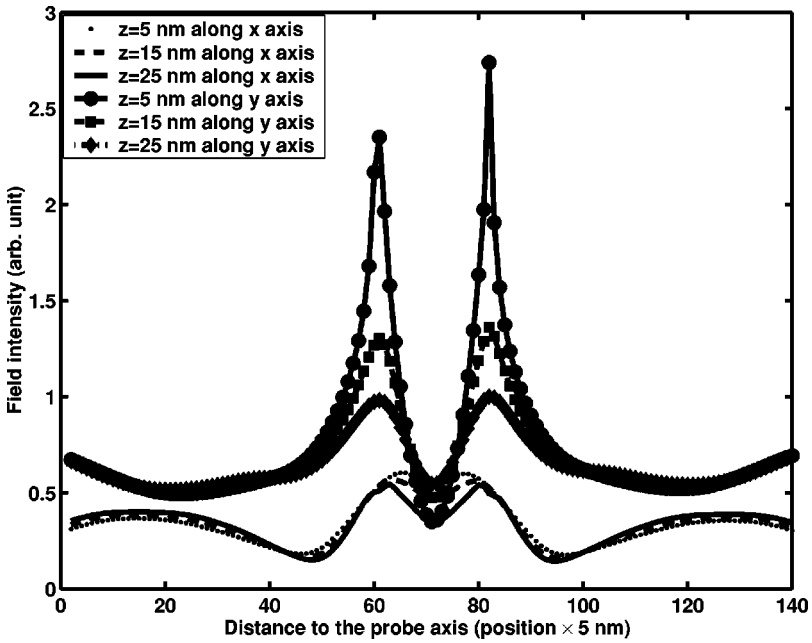

FIG. 6. Electric field distribution of the dielectric SIL probe along the x and y axis in the plane of $z=5$, 15, 25 nm, respectively.

taken into account. The spacing between the SIL probe and the recording layers is chosen as $h_2 = 50$ nm (see Fig. 1). The particular recording-layer structure investigated for the SIL-probe system recording is a four-layered medium:/ZnS–SiO_2 ($n = 2.15$, thickness $d = 90$ nm)/GeSbTe ($n_X = 4.45 + 1.65i$, $n_A = 4.4 + 2.1i$, thickness $d = 20$ nm)/ZnS–SiO_2 ($n = 2.15$, thickness $d = 15$ nm)/Al alloy ($n = 1.2 + 5.8i$, thickness $d = 150$ nm)/glass ($n = 1.5$), where n_X is the refractive index for the crystalline state and n_A is the refractive index for the amorphous state. The optical spot sizes and signal constrasts of this medium have been described for several conditions.[20] The scattered electric fields in time domain snap shot of $x-z$ (at $y = 61\Delta$) and $y-z$ sectional plane (at $x = 61\Delta$) are shown in Figs. 4(a) and 4(b), respectively. The dimension of each cell are $\Delta x = \Delta y = \Delta z = \Delta = 5$ nm, and the total space volume considered measures $121(x) \times 121(y) \times 151(z)$ cells. These results imply that the probe can work in the reflection-detection mode because of the scattered electric fields from the recorded mark can propagate into the probe. The steady state of electric field intensity plots of the $x-z$ sectional plane and $y-z$ sectional plane are illustrated in Figs. 5(a) and 5(b), respectively. The beam diameter (in $1/e^2$ maximum intensity) in the $x-z$ and $y-z$ sectional plane directions at the inside of the recording layers is 220 and 150 nm, respectively. These sizes are smaller than the wavelength light $\lambda = 633$ nm.

The more detailed calculation using the 3D FDTD method is shown in Fig. 6, which illustrates the beam profile along x and y axis in the plane of $z = 5$ nm, $z = 15$ nm, $z = 25$ nm from the exit surface of LaSFN9 glass probe, respectively. The results show that the outgoing light from the probe apex is weaker than that emitting from the lateral side and base of the SIL probe, and behaves as a strong contrast to the outgoing light of the probe apex. It implies that, for a dielectric SIL probe, propagating wave emitting from the intersection base of the SIL probe and from the conic side is stronger than that the outgoing light from the probe apex. It dominates the near-field distribution, while a film of metal is coated, the coated film can confine the light more strictly inside the probe tip and reduce the light of leakage from the SIL probe. The SIL-probe coated metallic film will provides a dramatic improvement in this regard. This will be understood in the Sec. III C.

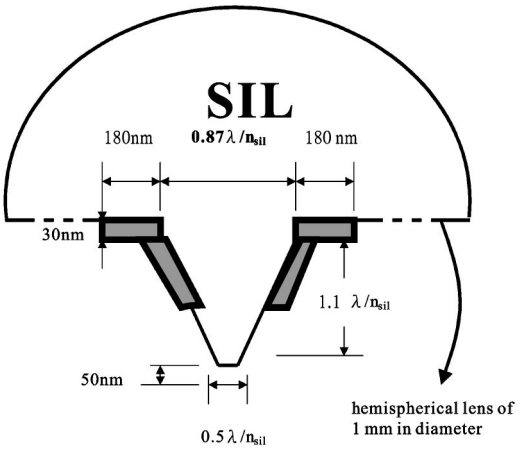

FIG. 7. The optimized geometry of the sectional diagram of the improved SIL-probe system.

C. A promising idea of fabricating a SIL-probe system

In the following, we will discuss one of the possible approaches and simulations about our idea of an optimal design of the SIL-probe system. It may be possible to fabricate a local metallic aperture in combination with a SIL. Experimental results show that the large background reflection from the metallic film that surrounds the apertures limit the detectable signal. Although the background reflection from the dielectric apertures is negligible, consider the aperture-only system where poor contrast is a result of the collection system not gathering enough spatial frequency information. Basically, laser light is focused by an objective lens onto a moving recording layer. The SIL probe which is in near contact with the recording layers, reduces the wavelength by a factor of n (refractive index of the SIL probe) and produces a small spot size. Reflected light is collected by the objective lens and directed to the detectors. The angular range of collected information is determined by the SIL probe, the objective lens, and the detector. If the angular range of collected information from the path between the recording layers and the SIL probe can be avoided by the light passing the metallic thin film, an optimal SIL probe with metallic film will be realized possibly. We can use both the advantage of high transmission efficiency with no ab-

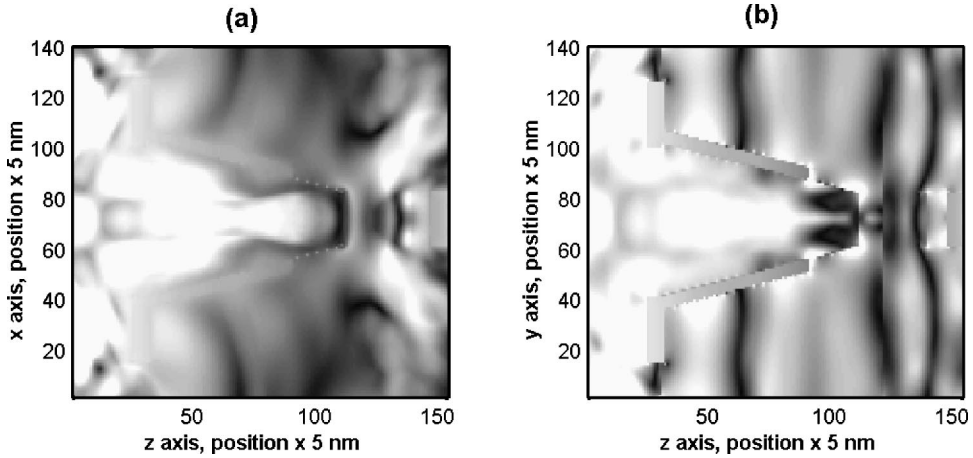

FIG. 8. The gray-scaled map of the total electric field modulus on the $x-z$ sectional plane (at $y = 71\Delta$) and $y-z$ sectional plane (at $x = 71\Delta$) for y-polarization illumination, respectively.

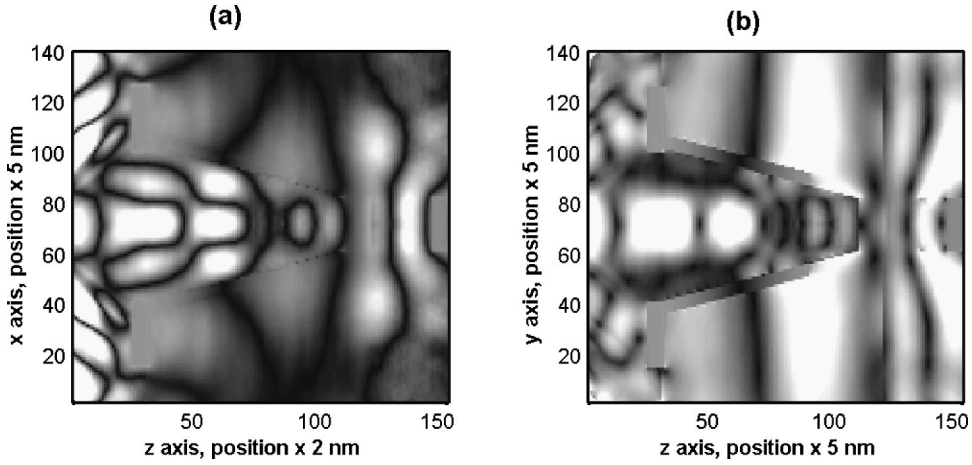

FIG. 9. The scattered electric fields in time domain snap shot of the $x-z$ (at $y=71\Delta$) and $y-z$ sectional plane (at $x=71\Delta$) are shown in Figs. 8(a) and 8(b), respectively.

sorption of the dielectric SIL probe and local enhancement of the metallic coating one (probe tip coated with metallic film which could be used to produce spots smaller than that generated with dielectric SIL-probe, but detection of the modulation is not efficient when uses it alone) to create a type of probe. Probe tips are fabricated directly on the bottom of a hemispherical SIL. The bottom face of SIL near to the entrance of probe is coated with aluminum film of 30 nm height with ring shape at the base of the SIL probe which external part and interior part are 480 and 300 nm, respectively. Detailed of the design and the fabrication process of dielectric aperture probe combined with the SIL are discussed in Refs. 21 and 22. Fabrication of our improved SIL-probe system is illustrated as following steps: (1) mount SIL-probe in carrier; (2) coat with photoresist; (3) expose photoresist to cross-grating pattern; (4) develop photoresist; and (5) metal coating. In the process of coating the aluminum thin film, we keep the tip apex exposed to fabricate a local uncoated metal tip. That is to say, the probe is based on the metal probe and extends the internal dielectric material outside the metal probe. In order to avoid the large background reflection from the metallic layer that surrounds the apertures limit the detectable signal, the length of the metallic coating must be short enough with the ratio to the SIL probe. So the background reflection from the metallic film in the reflection process can be neglected. Note that the incident light is accurately focused on the central part of the SIL bottom. The ratio to the length between the metallic film and the noncoated part of the probe is approximately 2:1. The diameter of the probe apex, the large end of the probe, and the height of the probe are approximately $0.3\lambda/n$, $0.87\lambda/n$, $1.1\lambda/n$ nm. The purpose of metallic coating is to conceal the lateral passing light and to enhance the field intensity locally inside the probe. Figure 7 shows a sectional diagram of a 3D FDTD model with recording layers of the improved probe to be analyzed. The dimension of each cell are $\Delta x=\Delta y=\Delta z=\Delta=5$ nm, and the total space volume considered measures $141(x)\times141(y)\times151(z)$ cells.

Here, let us choose the coordinate of probe apex to be $x=71\Delta$, $y=71\Delta$, $z=101\Delta$. Figure 8 shows the linear gray-scaled map of the total electric field modulus on the $x-z$ sectional plane (at $y=71\Delta$) and the $y-z$ sectional plane (at

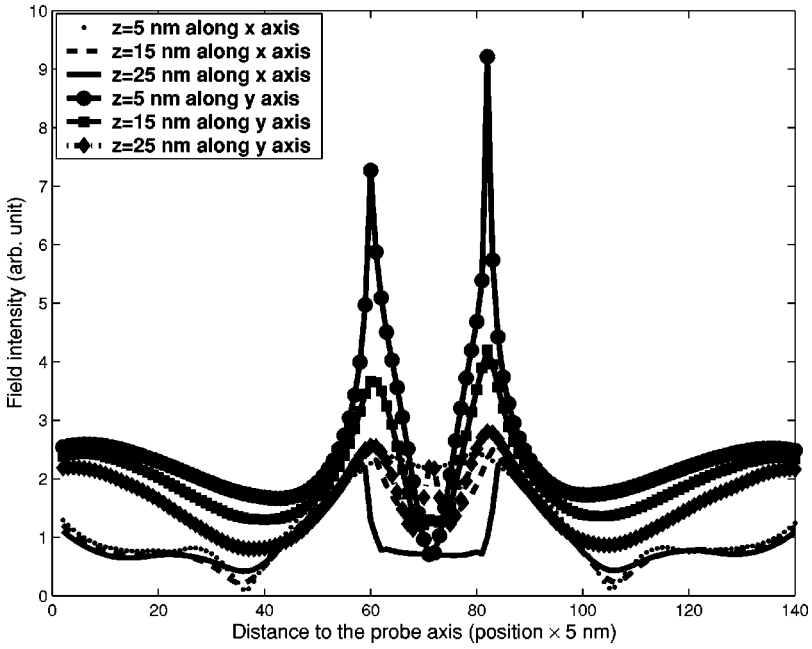

FIG. 10. Electric field distribution of the local metallic coating SIL-probe along the x and y axis in the plane of $z=5$, 15, 25 nm, respectively.

$x=71\Delta$) for y-polarization illumination, respectively. The scattered electric fields in time domain snap shot of $x-z$ (at $y=71\Delta$) and $y-z$ sectional plane (at $x=71\Delta$) are shown in Figs. 9(a) and 9(b), respectively. Figure 10 shows the electric field distribution of the local metallic coating SIL probe along the x and y axis in the plane of $z=5$, 15, 25 nm, respectively. Obviously, Fig. 10 compares with Fig. 6, the field intensity of improved probe is stronger than the dielectric probe at the border between dielectric and metal, but on the contrary at the center of the probe tip. We can regard the incident wave from the uncovered part of the improved SIL probe as the outgoing light passing through the dielectric one. This is to be expected since the propagating process in the uncovered part is similar to the dielectric SIL probe. In the sectional plane at $x=71\Delta$ ($y-z$ sectional plane), the light mainly escapes to the lateral side and has the strongest field intensity at the intersection place between dielectric and air. In the sectional plane at $y=71\Delta$ ($x-z$ sectional plane), the maximum distribution occurs along the z axis down to the probe tip.

IV. CONCLUSION

In this article, we report a series of 3D FDTD simulations to obtain more insight in the mechanisms responsible for the SIL-probe system in NSOM architecture and a promising idea to fabricate an optimal SIL-probe system is proposed. It is found that the electric field leaking from the base and conic side of the SIL-probe system is much stronger than the output of the probe apex. Our optimal SIL-probe system shows that the local metallic coating on the base of the SIL and the lateral side of the probe demonstrate high throughput and low reflection of the light beam compared with the conventional metal NSOM probe used only. The beam size inside the recording-layers, using the case of LaSFN9 glass, is estimated to be smaller than $(3/4)\lambda/n_{\text{sil-probe}}$ (in $1/e^2$ maximum intensity). The computed field from the recording layers supports the hypothesis that the optimal SIL probe which we have designed can work in the reflection-detection mode. In the near future, we intend to consider other detailed effects involving, e.g., the influences of taper angles, probe diameter, refractive index of inner dielectric material of the SIL probe, the polarization, focus positions, and the nonlinear response of the irradiated recording layers.

ACKNOWLEDGMENTS

The authors would like to thank National Chiao-Tung University for supporting the facility of PC computers. They want to acknowledge the National Science Council of Republic of China which offered them financial support through Grant No. NSC92-2112-M-009-023.

[1] E. Betzig, J. Trautman, R. Wolfe, E. Gyorgy, P. Finn, M. Kryder, and C. Chang, Appl. Phys. Lett. **61**, 142 (1992).
[2] Y. Martin, S. Rishton, and H. Wickramasinghe, Appl. Phys. Lett. **71**, 1 (1997).
[3] F. Issiki, K. Ito, K. Etoh, and S. Hosaka, Appl. Phys. Lett. **76**, 804 (2000).
[4] T. Yatsui, M. Kourogi, K. Tsutsui, M. Ohtsu, and J. Takahashi, Opt. Lett. **25**, 67 (2000).
[5] H. Yoshikawa, Y. Andoh, M. Yamamoto, K. Fukuzawa, T. Tamamura, and T. Ohkobo, Opt. Lett. **25**, 1296 (2000).
[6] B. D. Terris, H. J. Mamin, and D. Rugar, Appl. Phys. Lett. **68**, 141 (1995).
[7] B. D. Terris, H. J. Mamin, and D. Rugar, Appl. Phys. Lett. **65**, 388 (1994).
[8] T. Milster, K. Shimura, J. Jo, and K. Hirota, Opt. Lett. **24**, 605 (1999).
[9] L. P. Ghislain and V. B. Elings, Appl. Phys. Lett. **72**, 2779 (1998).
[10] K. Hirota, T. D. Milster, Y. Zhang, and J. K. Erwin, Jpn. J. Appl. Phys., Part 1 **39**, 973 (2000).
[11] A. Roberts, J. Appl. Phys. **65**, 2896 (1989).
[12] A. Roberts, J. Appl. Phys. **84**, 6485 (1998).
[13] R. Chang, P. K. Wei, W. S. Fann, M. Hayashi, and S. H. Lin, J. Appl. Phys. **81**, 3369 (1997).
[14] R. Muller and C. Lienaa, Appl. Phys. Lett. **74**, 976 (1995).
[15] K. S. Yee, IEEE Trans. Antennas Propag. **AP-14**, 302 (1966).
[16] A. Taflove, *Computational Electrodynamics: The Finite-Difference Time-Domain Method* (Artech House, Norwood, MA, 1995).
[17] K. S. Kunz and R. J. Luebbers, *The Finite Difference Time Domain Method for Electromagnetics* (CRC Press, Boca, Raton, 1993).
[18] H. Furukawa and S. Kawata, Opt. Commun. **132**, 170 (1996).
[19] L. Novotny, D. W. Pohl, and B. Hecht, Opt. Lett. **20**, 970 (1995).
[20] T. D. Milster, J. S. Jo, K. Hirota, and K. Shimura, in Digest of the International Symposium on Optical Memory, Tsukuba, 1998, paper Pd-15.
[21] Y. Zhang, K. Hirota, T. D. Milster, and J. K. Erwin, Jpn. J. Appl. Phys., Part 1 **39**, 973 (2000).
[22] T. D. Mister *et al.*, Jpn. J. Appl. Phys., Part 1 **40**, 1778 (2001).